

FlowLUT: Efficient Image Enhancement via Differentiable LUTs and Iterative Flow Matching

Liubing Hu, Chen Wu, Anrui Wang, Dianjie Lu, Guijuan Zhang, Zhuoran Zheng*

Abstract—Deep learning-based image enhancement methods face a fundamental trade-off between computational efficiency and representational capacity. For example, although a conventional three-dimensional Look-Up Table (3D LUT) can process a degraded image in real time, it lacks representational flexibility and depends solely on a fixed prior. To address this problem, we introduce FlowLUT, a novel end-to-end model that integrates the efficiency of LUTs, multiple priors, and the parameter-independent characteristic of flow-matched reconstructed images. Specifically, firstly, the input image is transformed in color space by a collection of differentiable 3D LUTs (containing a large number of 3D LUTs with different priors). Next, a lightweight fusion prediction network runs on multiple 3D LUTs, with $\mathcal{O}(1)$ complexity for scene-adaptive color correction. Furthermore, to address the inherent representation limitations of LUTs, we design an innovative iterative flow matching method to restore local structural details and eliminate artifacts. Finally, the entire model is jointly optimized under a composite loss function enforcing perceptual and structural fidelity. Extensive experimental results demonstrate the effectiveness of our method on three benchmarks.

Index Terms—Image enhancement, 3D LUTs, flow matching, computational efficiency, real-time processing.

I. INTRODUCTION

HIGH quality image is critical for both human visual perception and downstream computer vision tasks [1], including object detection [2], semantic segmentation [3], and autonomous driving [4]. However, deep learning-based image enhancement methods, especially for resource-constrained platforms [5], face a fundamental dilemma: balancing computational efficiency and representational capacity.

Currently, in pursuit of extreme computational efficiency, researchers widely employ three-dimensional Look-Up Tables (3D LUTs) as a core technique [7]. They enable constant-time ($\mathcal{O}(1)$) pixel mapping [6] via sparse sampling and trilinear interpolation [8], making them ideal for real-time pipelines.

Liubing Hu is with School of Engineering, Zhejiang Normal University, Jinhua 321004 China (e-mail: hlb0699@zjnu.edu.cn).

Chen Wu is with School of Computer Science and Engineering, University of Science and Technology of China, Hefei 230000 China (e-mail: wuchen5X@mail.ustc.edu.cn).

Anrui Wang is with School of Computer Science and Engineering, Nanjing University of Science and Technology, Nanjing 210094 China (e-mail: wangar@njust.edu.cn).

Dianjie Lu is with School of Information Science and Engineering, Shandong Normal University, Jinan 250399 China (e-mail: ludianjie@sdnu.edu.cn).

Guijuan Zhang is with School of Information Science and Engineering, Shandong Normal University, Jinan 250399 China (e-mail: zhangguijuan@sdnu.edu.cn).

Zhuoran Zheng is with School of Computer Science and Engineering, Nanjing University of Science and Technology, Nanjing 210094 China (e-mail: zhengzr@njust.edu.cn).

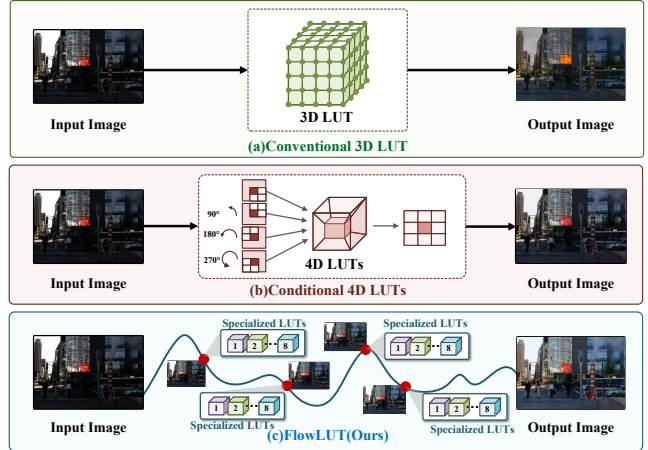


Fig. 1. This figure illustrates the advantages of our method, which gradually transfers the image distribution to the correct domain using vector fields. In contrast, traditional 3D and 4D LUT algorithms transfer the distribution in bulk using inherent parameters, which clearly lacks representational ability.

Recent advances employ lightweight CNNs to predict adaptive LUT contents or fusion weights [9], [19], enhancing scene adaptability while preserving efficiency. Unfortunately, all LUT-based methods suffer from inherent spatial invariance: identical RGB inputs yield identical outputs regardless of location. This limits their ability to correct spatially unique degradations (e.g., local exposure errors), restore fine textures, or handle complex illumination [10]. While spatial awareness has been attempted via bilateral grids [11] or per-pixel weighting, these approaches compromise the core efficiency advantage of LUTs.

In contrast to LUT-based methods, recent flow matching techniques, such as Flow-GRPO [12] and MeanFlow [13], have emerged as a highly attractive alternative, demonstrating exceptional performance in image restoration tasks. These methods excel at modeling complex, spatially varying transformations. For instance, Flow-GRPO [12] introduces an online reinforcement learning framework to precisely guide the transformation path, proving highly effective in restoring complex, non-uniform degradations. Meanwhile, MeanFlow [13] simplifies the generation process into a single, efficient step by directly modeling the mean of the conditional flow, achieving state-of-the-art results in generation tasks. These advancements enable flow matching to effectively handle local degradations and restore fine details that are intractable for traditional LUTs. A key advantage is their computational efficiency; well-designed flow operations can achieve favorable computational complexity compared to

heavy CNNs [14] or Transformers [15], making them suitable for real-time applications. Despite this success, a critical challenge remains: designing an image enhancement framework that can synergize the $\mathcal{O}(1)$ efficiency of LUTs with the powerful spatial adaptability and restoration capabilities of flow-based methods, thereby resolving the long-standing trade-off between computational speed and high-fidelity, spatially-aware image restoration.

As shown in Fig. 1, to resolve the issue, we propose FlowLUT, an end-to-end trainable image enhancement architecture. FlowLUT synergizes Look-Up Table (LUT) and flow matching strengths within a unified two-stage framework, balancing performance and efficiency [17]. First, We employ a differentiable 3D LUTs module, incorporating physically-inspired priors to guide initial learning effectively. Next, a lightweight content-aware network then dynamically predicts fusion weights, enabling scene-adaptive global color correction with $\mathcal{O}(1)$ complexity. Then, a novel Flow Matching Module is introduced to restore local details and eliminate artifacts. Its core innovation is the gradient-preserving residual alignment mechanism. Finally, applied additively to the LUT-enhanced image, this mechanism predicts a Residual Correction Field instead of performing direct spatial warping [16]. This design ensures direct gradient propagation during training, significantly stabilizing end-to-end optimization while enabling precise local refinement. The main contributions of our work are summarized as follows:

- We propose FlowLUT, a novel end-to-end method that synergistically unifies the $\mathcal{O}(1)$ efficiency of 3D LUTs with the spatial refinement capability of flow-based methods, effectively addressing the long-standing trade-off between computational efficiency and representational capacity in image enhancement.
- We design an efficient Global Enhancement Stage incorporating a specialized, physically inspired 3D LUT integration module and a lightweight content-aware network for dynamically generating scene-adaptive fusion weights, allowing the model to intelligently blend these transformations for superior global enhancement.
- We introduce an innovative Gradient-Preserving Flow Matching Module that performs local refinement via additive residual correction, enabling stable end-to-end optimization while achieving state-of-the-art quantitative and qualitative results across multiple benchmarks with significant gains in both perceptual quality and computational efficiency.

II. RELATED WORK

Look-up table-based image enhancements. The application of three-dimensional Look-Up Tables (3D LUTs) for image enhancement has long been favored in industrial pipelines due to its exceptional computational efficiency [6], [11]. By pre-calculating color transformations on a sparse grid and applying trilinear interpolation, 3D LUTs achieve real-time, resolution-independent color mapping with constant-time ($\mathcal{O}(1)$) complexity. However, traditional LUTs are static and lack content-awareness, applying a fixed transformation

irrespective of image semantics. To overcome this rigidity, recent research has focused on making LUTs adaptive. A prominent direction involves using lightweight Convolutional Neural Networks (CNNs) to dynamically generate the contents of a 3D LUT or predict its parameters based on the input image. For instance, Zeng et al. [6] pioneered an end-to-end framework that learns an image-adaptive 3D LUT for high-performance photo enhancement. Subsequent works have sought to improve the flexibility and efficiency of this paradigm. Yang et al. [9] proposed AdaInt, which learns adaptive intervals for LUT grids to achieve a better trade-off between performance and efficiency. Concurrently, methods like SepLUT [19] decompose a 3D LUT into three 1D LUTs to reduce parametric complexity. Other approaches, such as that by Wang et al. [10], learn to predict weights to fuse a small bank of pre-defined or learned LUTs, expanding the expressiveness of the transformation space. Although LUT and its enhanced versions perform well, their performance in complex scenes is poor due to their fixed projection method. **Flow matching for visual task.** Flow matching has recently emerged as a simple yet powerful framework for generative modeling, enabling simulation-free training of continuous normalizing flows (CNFs) with enhanced efficiency and stability compared to traditional diffusion-based training [21]. Its efficacy has been demonstrated across a multitude of domains, pushing state-of-the-art performance in large-scale applications such as high-resolution image synthesis [22], [23], audio synthesis [24], and 3D point cloud processing [26]. UniFlowRestore [27], based on flow matching and prompt guidance, models video restoration as the continuous evolution of a physical vector field, achieving a unified restoration framework for multiple tasks [25]. In the realm of image restoration, flow-based methods have proven highly effective at modeling complex, spatially-varying transformations, a task where spatially-invariant operators like traditional LUTs often fall short [12]. Recent advancements like rectified and mean flows have further boosted their efficiency and performance [28]. Building on the success of flow matching across various domains, our framework, FlowLUT, introduces a novel synergy by leveraging flow matching for local refinement.

III. PROPOSED METHOD

A. Overview

As illustrated in Fig. 2, FlowLUT is an end-to-end image enhancement framework that combines the efficiency of 3D Look-Up Tables (LUTs) with the precision of flow-based local refinement. The method begins with global color correction, where a lightweight dynamically generates content-aware weights to fuse transformations from a bank of specialized, differentiable 3D LUTs, adapting the correction to the specific image. Subsequently, an iterative flow matching module refines the image by applying residual corrections to restore local details and structural integrity, overcoming the spatial limitations of traditional LUTs. Our method tradeoff computational speed with high perceptual quality and is optimized jointly to ensure both color fidelity and structural preservation.

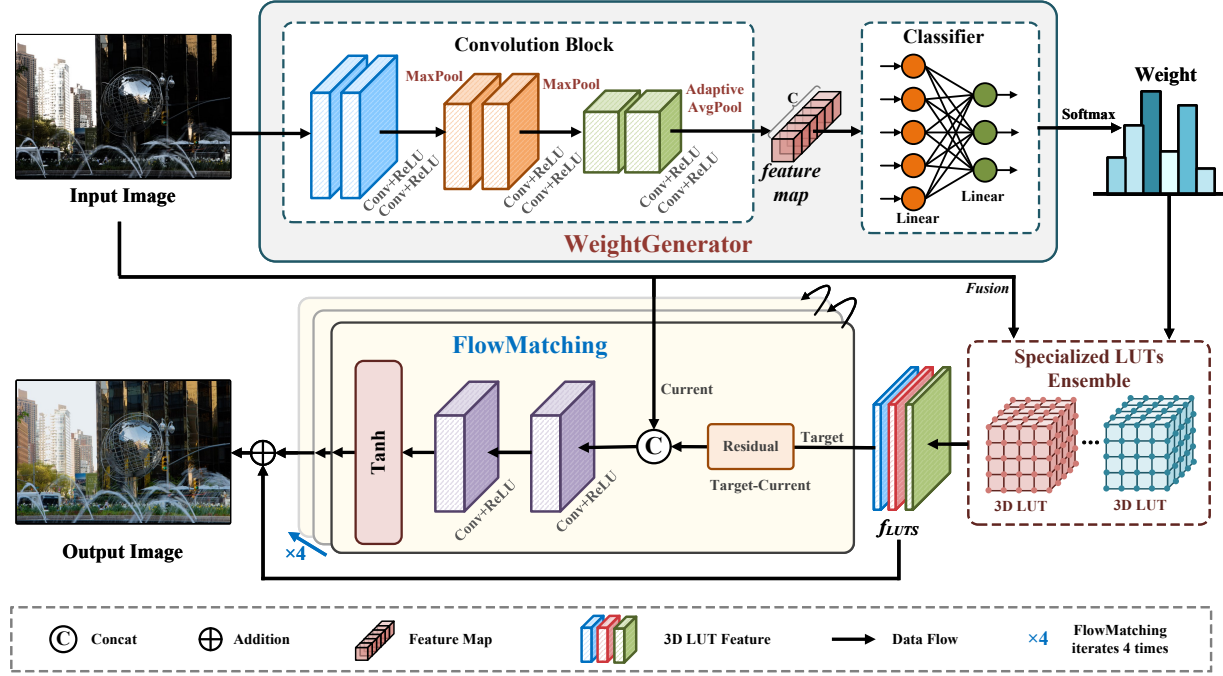


Fig. 2. The architecture of the proposed FlowLUT. Our method is composed of three key components: a lightweight weightgenerator, a specialized LUTs ensemble, and an iterative flow matching module. Our method begins with the weightgenerator supplying content-aware weights to the LUT ensemble for global, scene-adaptive color correction. Next, the iterative flow matching module predicts a residual correction field to restore local details and remove artifacts. This iterative refinement converges after a fixed number of steps, yielding a high-quality final image.

B. Initialize specialized LUTs

The LUT ensemble forms the global color transformation stage, constructed as a bank of N differentiable 3D LUTs ($N = 8$ in our implementation). Each LUT, denoted as L_i , acts as a function mapping an input RGB value to an output RGB value within the normalized RGB space. Specifically, each LUT is a discretized 3D grid of size $D \times D \times D$. At each grid point (i, j, k) , a 3-dimensional RGB color vector is stored. Consequently, the parameters of each LUT are represented by a tensor of size $D \times D \times D \times 3$, where we set the lattice dimension $D = 33$ in our implementation.

We initialize a set of Look-Up Tables (LUTs) using physically-inspired, differentiable transformations to establish meaningful priors for optimization. These operations are applied to normalized RGB color coordinates, denoted as $\mathbf{p} = [p_r, p_g, p_b]^T$. The set includes a baseline identity LUT (L_0), which performs no transformation, and a contrast enhancement LUT (L_1) that applies gamma correction to the image. For color temperature adjustments, a warm tone LUT (L_2) increases red channel values while decreasing blue, and a cool tone LUT (L_3) does the reverse. The vibrancy of the color is manipulated through a saturation boost LUT (L_4) that works by amplifying the saturation component in the HSV color space. The set is further complemented by a brightness boost LUT (L_5) for uniform increases in luminance, a sinusoidal S-curve LUT (L_6) for non-linear tonal adjustment, and a final inversion LUT (L_7) that inverts the image colors.

We implement LUTs using differentiable trilinear interpolation for a given input coordinate $\mathbf{p} \in [0, 1]^3$. The process begins by scaling the coordinates $\mathbf{p}' = \mathbf{p} \times (\mathbf{D} - 1)$ based on the lattice dimension $\mathbf{D} = 33$. Subsequently, the

integer and fractional parts of the scaled coordinates are computed ($\mathbf{i} = \lfloor \mathbf{p}' \rfloor$, $\mathbf{f} = \mathbf{p}' - \mathbf{i}$) to fetch the corresponding corner values ($V_i = L[\mathbf{i}]$) from the LUT. Finally, these corner values are used to perform trilinear interpolation¹, yielding the output.

C. LUTs fusion

The adaptive weight generation network serves as the decision-making core of FlowLUT, dynamically predicting content-dependent fusion weights for the specialized LUTs. The weight generator network comprises three stages:

Multi-scale feature extraction. The weight generator network first processes the input image $\mathbf{I} \in \mathbb{R}^{3 \times H \times W}$ through a three-block convolutional backbone to extract multi-scale features. Each block consists of two 3×3 convolutional layers followed by a 2×2 max-pooling layer for spatial downsampling. The process is formulated as follows:

Let $\mathbf{F}_0 = \mathbf{I}$ be the input. For each block $k \in \{1, 2, 3\}$, the operations are defined as:

$$\mathbf{F}'_k = \text{ReLU} \left(\text{Conv}_{C_k \rightarrow C_k} \left(\text{ReLU} \left(\text{Conv}_{C_{k-1} \rightarrow C_k} (\mathbf{F}_{k-1}) \right) \right) \right), \quad (1)$$

$$\mathbf{F}_k = \text{MaxPool}(\mathbf{F}'_k), \quad (2)$$

where $\text{Conv}_{C_{\text{in}} \rightarrow C_{\text{out}}}$ denotes a 3×3 convolution, and MaxPool is a max-pooling operation with a stride of 2. The channel dimensions are set to $C_0 = 3$, $C_1 = 64$, $C_2 = 128$, and $C_3 = 256$. Finally, we obtain the output feature map from

¹Gonzalez, R. C., & Woods, R. E. (2008). Digital Image Processing. Prentice Hall.

the third block before its pooling layer as $F_3 \in \mathbb{R}^{256 \times \frac{H}{4} \times \frac{W}{4}}$, which then proceeds to the global context aggregation stage. **Global context aggregation.** To generate image-level weights invariant to spatial arrangement, we apply adaptive average pooling:

$$\mathbf{F}_{\text{global}} = \text{AdaptiveAvgPool2d}(1)(\mathbf{F}_3). \quad (3)$$

This operation compresses the 256-channel feature map $\mathbf{F}_3 \in \mathbb{R}^{256 \times \frac{H}{4} \times \frac{W}{4}}$ into a 256-dimensional vector $\mathbf{F}_{\text{global}} \in \mathbb{R}^{256}$ encapsulating the image's global properties.

Weight prediction. The weight prediction is a two-stage process. First, a global descriptor is projected into an intermediate feature space:

$$\mathbf{W}_{\text{raw}} = \text{ReLU}(\text{Linear}_1(\mathbf{F}_{\text{global}})). \quad (4)$$

Then, a second linear layer projects this feature vector to a dimensionality of N (corresponding to the N LUTs), followed by a Softmax function to generate the final fusion weights w :

$$w = \text{Softmax}(\text{Linear}_N(\mathbf{W}_{\text{raw}})), \quad (5)$$

where Linear_1 and Linear_N represent two distinct linear layers. The output of Linear_N is a logit vector of size N , which is then passed to a Softmax function. The resulting vector $w = [w_1, w_2, \dots, w_N]^T$ represents the fusion weights for the N LUTs. The softmax operation ensures $\sum_{i=1}^N w_i = 1$ and $w_i \geq 0$, guaranteeing physically plausible blending. The predicted weights w then modulate the LUT ensemble through differentiable blending:

$$\mathbf{I}_{\text{LUT}} = \sum_{i=1}^N w_i \cdot L_i(\mathbf{I}). \quad (6)$$

D. Flow matching refinement

Our method introduces an iterative flow-based refinement that progressively aligns local features between the LUT-enhanced image and the original input, restoring structural integrity while preserving color fidelity.

Iterative residual flow. Given the LUT-enhanced image \mathbf{I}_{LUT} and original input \mathbf{I}_{in} , we formulate refinement as a multi-step alignment process:

$$\mathbf{I}_{\text{refined}}^{(0)} = \mathbf{I}_{\text{LUT}}, \quad (7)$$

For $k = 1$ to K :

$$\mathbf{R}^{(k)} = \mathbf{I}_{\text{in}} - \mathbf{I}_{\text{refined}}^{(k-1)}, \quad (8)$$

$$\Delta \mathbf{F}^{(k)} = \mathcal{F}_{\theta} \left(\text{Concat} \left(\mathbf{I}_{\text{refined}}^{(k-1)}, \mathbf{R}^{(k)} \right) \right), \quad (9)$$

$$\mathbf{I}_{\text{refined}}^{(k)} = \mathbf{I}_{\text{refined}}^{(k-1)} + \frac{1}{K} \cdot \Delta \mathbf{F}^{(k)}, \quad (10)$$

where \mathcal{F}_{θ} denotes the flow prediction network, $\mathbf{R}^{(k)}$ is the residual map at step k , and $\Delta \mathbf{F}^{(k)} \in [-1, 1]^{3 \times H \times W}$ represents the predicted flow field. The $\frac{1}{K}$ factor ensures gradual convergence while preventing overshooting.

Flow prediction network. The core component \mathcal{F}_{θ} employs a lightweight CNN architecture with the following mathematical formulation:

$$\mathcal{F}_{\theta}(\mathbf{X}) = \text{Tanh}(\text{Conv}(\text{ReLU}(\text{Conv}(\text{ReLU}(\text{Conv}(\mathbf{X})))))). \quad (11)$$

The architecture comprises an initial input layer, which is a 6-channel tensor $\mathbf{X} \in \mathbb{R}^{6 \times H \times W}$ formed by concatenating $I_{\text{refined}}^{(k-1)}$ and $R^{(k)}$. Subsequently, for feature extraction, the input tensor is processed by a first convolution, $\text{Conv}_{64} : \mathbb{R}^{6 \times H \times W} \rightarrow \mathbb{R}^{64 \times H \times W}$, followed by a second convolution, $\text{Conv}_{64} : \mathbb{R}^{64 \times H \times W} \rightarrow \mathbb{R}^{64 \times H \times W}$. Following this, the flow prediction is accomplished through a final convolution, $\text{Conv}_3 : \mathbb{R}^{64 \times H \times W} \rightarrow \mathbb{R}^{3 \times H \times W}$. Finally, a Tanh nonlinearity is applied for activation, constraining the output to the range of $[-1, 1]$. All convolutional layers utilize 3×3 kernels with padding=1 to maintain the spatial dimensions. This design achieves effective spatial refinement with only 42,179 parameters (0.042M), thereby maintaining the framework's efficiency while expanding the effective receptive field to 7×7 pixels through the successive convolutions. Ultimately, an enhanced image \mathbf{I}_{out} is produced as the output through flow matching.

E. Loss functions

The optimization of FlowLUT employs a multi-objective loss function that simultaneously enforces color fidelity and perceptual quality. This composite loss addresses the dual nature of image enhancement tasks, where both pixel-level accuracy and high-level perceptual quality are critical for human visual satisfaction. The loss formulation is defined as: The composite loss function integrates two complementary objectives:

$$\mathcal{L}_{\text{total}} = \underbrace{\mathcal{L}_{\text{MSE}}}_{\text{Pixel fidelity}} + 0.1 \cdot \underbrace{\mathcal{L}_{\text{LPIPS}}}_{\text{Perceptual quality}}. \quad (12)$$

Pixel-level fidelity loss. The Mean Squared Error (MSE) loss ensures basic color accuracy and serves as the foundational optimization objective. The Mean Squared Error loss ensures color accuracy:

$$\mathcal{L}_{\text{MSE}} = \frac{1}{CHW} \sum_{c=1}^C \sum_{i=1}^H \sum_{j=1}^W \|\mathbf{I}_{\text{out}}(i, j, c) - \mathbf{I}_{\text{gt}}(i, j, c)\|_2^2, \quad (13)$$

where \mathbf{I}_{out} is the enhanced image, \mathbf{I}_{gt} is the ground truth, and C, H, W denote channel, height, and width dimensions.

Perceptual quality loss. To better align the enhancement results with human visual perception [32], which is often sensitive to textural and structural similarities rather than just pixel-wise errors, we employ the learned perceptual image patch similarity (LPIPS [38]) metric as a loss function. Unlike a standard VGG-based loss that computes a simple Euclidean distance between feature maps, LPIPS is a calibrated metric. It computes distances in the feature space of a VGG-16 network and uses a set of pre-calibrated linear weights to better correlate with human perceptual judgments. The LPIPS loss is formulated as:

$$\mathcal{L}_{\text{LPIPS}}(\mathbf{I}_{\text{out}}, \mathbf{I}_{\text{gt}}) = \sum_l w_l \cdot \|\hat{h}_l(\phi^l(\mathbf{I}_{\text{out}})) - \hat{h}_l(\phi^l(\mathbf{I}_{\text{gt}}))\|_2^2 \quad (14)$$

where ϕ^l denotes the feature activations from layer l of the VGG network, \hat{h}_l is a channel-wise normalization operation, and w_l are the learned linear weights that scale the contribution of each layer. This approach provides a more robust measure

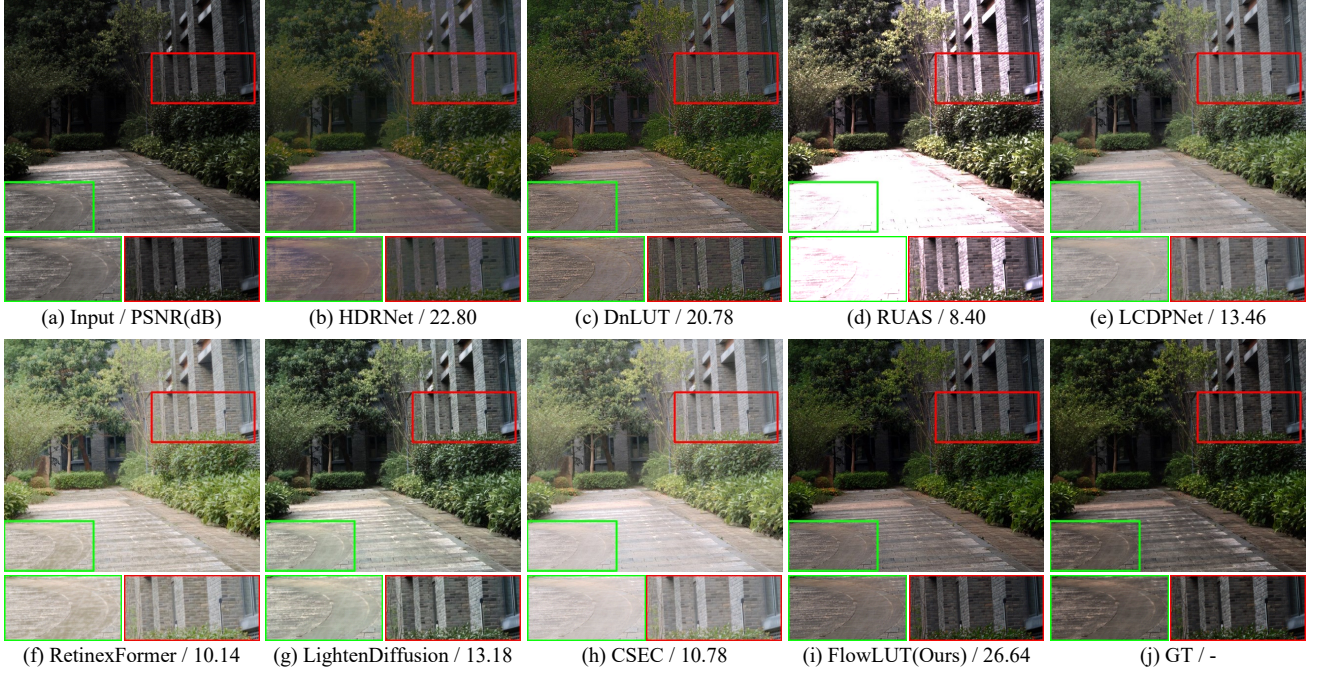


Fig. 3. Visual comparison on the Mobile-spec dataset. It highlights that our method, FlowLUT, achieves superior image restoration performance, as demonstrated by its ability to generate images with higher PSNR values compared to other methods.

TABLE I

COMPARISON OF QUANTITATIVE RESULTS ON LCDP, MOBILE-SPEC, AND LSUI DATASETS. THE BEST AND SECOND-BEST VALUES ARE MARKED IN **BOLD** AND UNDERLINE RESPECTIVELY.

Methods	Venue & Year	LCDP				Mobile-spec				LSUI			
		PSNR \uparrow	SSIM \uparrow	LPIPS \downarrow	CIEDE \downarrow	PSNR \uparrow	SSIM \uparrow	LPIPS \downarrow	CIEDE \downarrow	PSNR \uparrow	SSIM \uparrow	LPIPS \downarrow	CIEDE \downarrow
HDRNet	SIGGRAPH'17	22.09	0.8088	0.1773	14.23	20.34	0.7991	0.1652	6.57	18.22	0.7097	0.2817	20.98
RUAS	CVPR'21	13.93	0.6280	0.3100	15.03	12.22	0.7470	0.1833	17.26	15.13	0.7084	0.3702	33.17
LCDPNet	ECCV'22	23.24	0.8416	0.1632	<u>7.10</u>	20.71	0.7954	0.1546	13.69	19.56	0.7583	0.3273	24.88
AdaInt	CVPR'22	21.63	0.8329	0.1892	9.85	21.09	0.7869	0.1623	15.61	17.86	0.7693	0.2867	22.58
RetinexFormer	ICCV'23	<u>23.51</u>	<u>0.8549</u>	<u>0.1556</u>	10.02	23.72	0.8429	<u>0.1452</u>	20.54	16.35	0.6808	0.2842	21.05
LightenDiffusion	ECCV'24	20.03	0.8012	0.3021	11.98	18.43	0.7808	0.1990	25.74	18.28	0.5825	0.2927	18.74
CSEC	CVPR'24	23.35	0.8552	0.1563	7.93	21.92	0.7953	0.1632	22.79	19.89	0.7645	0.2678	24.20
CE-VAE	WACV'24	-	-	-	-	-	-	-	-	<u>24.49</u>	<u>0.8445</u>	<u>0.2622</u>	<u>7.98</u>
DnLUT	CVPR'25	21.02	0.7563	0.3002	8.68	<u>23.85</u>	0.8326	0.1856	<u>6.16</u>	19.23	0.7256	0.2796	10.36
FlowLUT (Ours)	-	23.85	0.8789	0.1328	6.30	26.66	0.9335	0.0850	3.90	25.75	0.8861	0.1883	6.78

of perceptual quality, guiding the model to produce visually pleasing results.

IV. EXPERIMENTS

A. Datasets

LCDP dataset [33]. To train and evaluate our proposed method, we conduct experiments using the exposure dataset. Specifically, the LCDP dataset comprises images containing both overexposed and underexposed regions, making it well-suited for evaluating our method’s ability to handle these challenging conditions effectively. The LCDP dataset consists of 1,733 images, which are split into 1,415 for training, 100 for validation, and 218 for testing.

Mobile-Spec dataset [34]. The Mobile-Spec dataset is a high-quality collection combining RGB images captured by high-end smartphones with images acquired using the GaiaSky-mini2 hyperspectral camera. It is specifically designed to facilitate research on image enhancement and related applications

in mobile photography. The dataset includes 160 images for training and 40 for testing.

LSUI dataset [36]. To evaluate the effectiveness of our method in image color correction, we also perform experiments on the synthetic underwater enhanced image dataset LSUI. The dataset is divided into 3,879 images for training and 400 images for testing.

B. Implementation details

We conduct these experiments using PyTorch on a single NVIDIA RTX4090 24GB GPU. During training, we resize the input images to 256×256 and use a batch size of 8. To optimize the network, we employ the AdamW optimizer with a learning rate $1e^{-4}$, and momentum terms of (0.9, 0.999), and train the model for 150 epochs. Additionally, in our FlowLUT, we set the number of specialized 3D LUTs to 8, with each of size $33 \times 33 \times 33 \times 3$. The flow matching step is set to 4. For testing, we evaluate performance using three

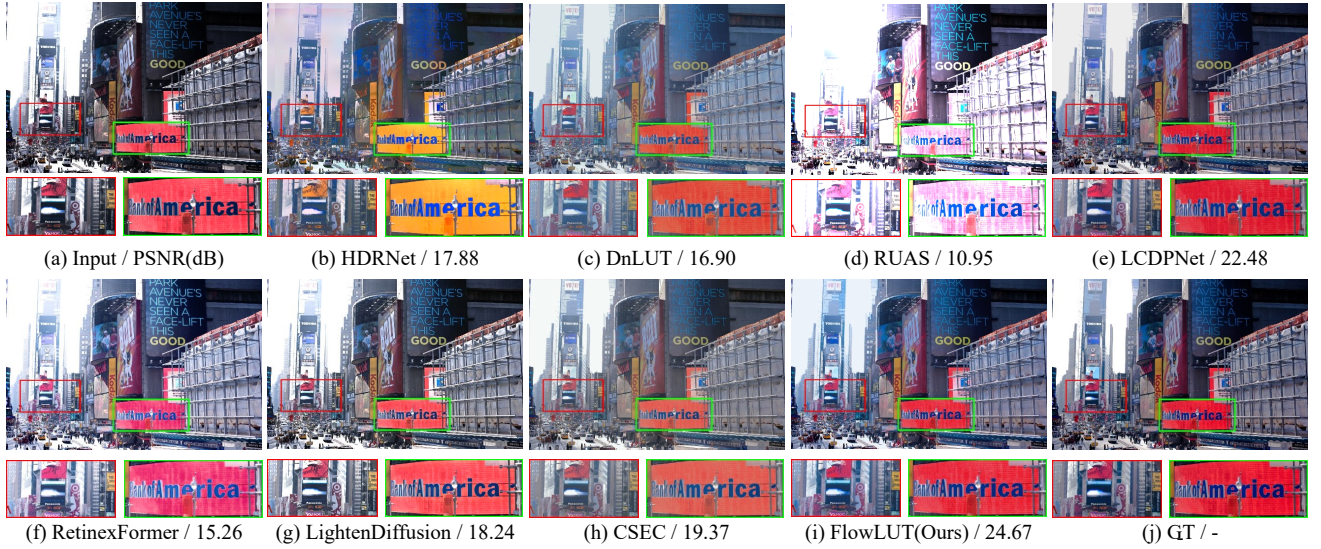


Fig. 4. Visual comparison on the LCDP dataset. Our method, FlowLUT, demonstrates a clear superiority over all state-of-the-art methods by excelling in the challenging task of simultaneous exposure restoration. It faithfully reconstructs intricate details from deep shadows and vibrant colors from saturated highlights, resulting in a more natural, balanced, and visually superior outcome where other methods often struggle.

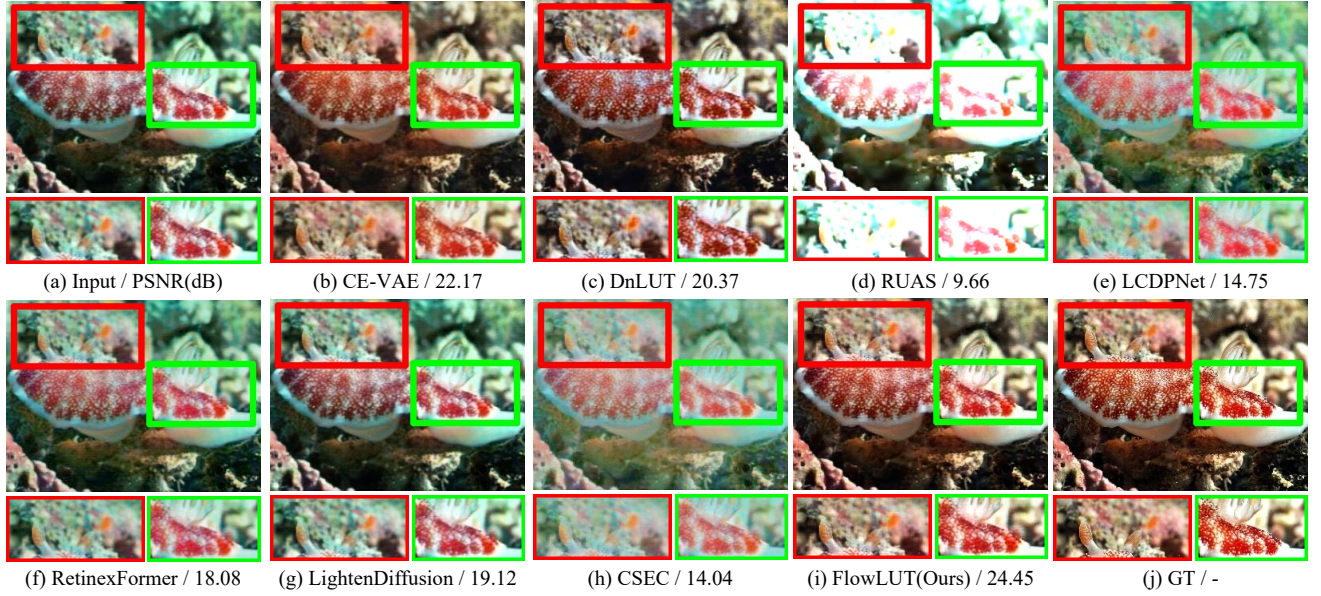


Fig. 5. Visual comparison on the LSUI dataset. It demonstrated that our method, FlowLUT, achieves remarkable performance in underwater image restoration, effectively enhancing details and preserving color accuracy in challenging underwater environments.

widely recognized metrics: PSNR, SSIM [37], LPIPS [38], and CIEDE 2000 [40].

C. Quantitative results

To demonstrate the superiority of our proposed FlowLUT, we conduct a comprehensive comparative analysis against several state-of-the-art (SOTA) image enhancement methods. The evaluation includes the classic method HDRNet [11], leading low-light image enhancement models like RUAS [41], and the Transformer-based RetinexFormer [42], as well as recent approaches for over and under exposure correction, namely LUT-based methods AdaInt [9], DnLUT [43], a diffusion model LightenDiffusion [44], and other strong baselines LCDPNet [33], and CSEC [45]. Furthermore, to assess its applicability in specialized scenarios, FlowLUT is benchmarked

against the SOTA underwater image enhancement method, CE-VAE [46]. These methods were fine-tuned on the evaluation dataset and employed data augmentation techniques. As shown in Table I, FlowLUT consistently outperforms existing state-of-the-art methods across all three benchmark datasets (LCDP, Mobile-spec, and LSUI). Notably, FlowLUT achieves the highest scores in both PSNR and SSIM metrics while simultaneously attaining the lowest (best) LPIPS and CIEDE2000 values, demonstrating its superior performance in both pixel-level accuracy and perceptual quality. Collectively, these results underscore the robustness and superior capability of our method in enhancing image quality across diverse and challenging scenarios, including overexposed, underexposed, and underwater conditions.

TABLE II

ABLATION STUDY OF THE KEY COMPONENTS ON THE MOBILE-SPEC DATASET. THE FLOWLUT (GROUP E) INCLUDES ALL PROPOSED COMPONENTS. WE REPORT RESULTS ON THE MOBILE-SPEC DATASET. THE BEST PERFORMANCE FOR EACH METRIC IS MARKED IN **BOLD**.

Group	Specialized LUTs	Flow Matching	LPIPS Loss	LUT Init	PSNR \uparrow	SSIM \uparrow	LPIPS \downarrow	CIEDE \downarrow
(a)		✓	✓		21.55	0.7511	0.1363	7.0798
(b)	✓		✓	✓	21.82	0.7628	0.1224	6.8737
(c)	✓	✓		✓	24.75	0.8724	0.1445	5.4186
(d)	✓	✓	✓		25.09	0.8899	0.0996	5.5335
(e)	✓	✓	✓	✓	26.66	0.9335	0.0850	3.9049

TABLE III

ABLATION STUDY ON THE NUMBER OF LUTS AND THE NUMBER OF FLOW MATCHING STEPS.

num_luts	flow_steps	PSNR \uparrow	SSIM \uparrow	LPIPS \downarrow	CIEDE \downarrow
4	4	25.24	0.8922	0.0982	5.1092
6	4	25.91	0.8957	0.1025	4.7175
10	4	23.59	0.8864	0.1215	5.9750
12	4	25.12	0.8907	0.1056	5.2155
8	3	25.11	0.8925	0.0937	5.2452
8	5	25.46	0.9162	0.1009	4.7818
8	6	26.02	0.8906	0.0863	4.5353
8	7	25.04	0.8896	0.0949	5.5874
8	4	26.66	0.9335	0.0850	3.9049

D. Qualitative results

To further substantiate the quantitative metrics, this section provides a visual comparison between our proposed FlowLUT and other state-of-the-art methods across various challenging datasets.

As shown in Fig. 3, Fig. 3(a) is severely underexposed, rendering the walkway texture indistinct and losing the building's stonework completely in shadow. Methods like Fig. 3(b) and Fig. 3(c) manage to brighten the scene but produce muted colors and fail to restore the fine texture on the walkway. Fig. 3(d) fails catastrophically, blowing out the highlights on the path into a washed-out patch and creating severe artifacts. Other methods, such as Fig. 3(h) and Fig. 3(f), leave a hazy, grayish cast over the image, failing to restore natural color fidelity. In contrast, Fig. 3(i) successfully reveals the detailed texture of the stone path, restores the vibrant and natural green of the foliage, and renders a result with balanced lighting that is remarkably close to Fig. 3(j).

Fig. 4 presents a case of extreme overexposure, where the Fig. 4(a) features a completely white sky and washed-out, illegible text on the billboards. Most approaches, including the Fig. 4(b) and the Fig. 4(g), are unable to recover the lost color information, resulting in a dull and hazy appearance where the vibrant red sign appears orange. While the Fig. 4(e) performs better than most, the iconic red sign still appears muted and lacks vibrancy. Our method, the Fig. 4(i), demonstrates superior performance by effectively mitigating the overexposure. It not only restores the deep blue of the sky but also recovers the sharp text on the billboards and, crucially, renders the "Bank of America" sign in its correct, vibrant red, closely matching the Fig. 4(j).

Finally, Fig. 5 demonstrates FlowLUT's effectiveness on the LSUI underwater dataset. The Fig. 5(a) suffers from a dominant blue-green color cast and low contrast, typical of underwater environments. While the Fig. 5(b) offers some improvement, it fails to fully neutralize the color cast. Other

general-purpose methods produce results with significant color distortion Fig. 5(d, e, h) or insufficient correction Fig. 5(c, f, g). The Fig. 5(i) stands out by successfully removing the color cast, enhancing contrast, and restoring the intricate details and natural reddish hues of the coral.

Collectively, these visual comparisons in Fig. 3, 4, and 5 underscore the robustness and versatility of FlowLUT. Our method consistently outperforms existing approaches in diverse and difficult scenarios, including extreme low-light, severe overexposure, and challenging underwater conditions [35], demonstrating a superior ability to achieve both accurate color correction and high-fidelity detail restoration.

E. Ablation Studies

We perform ablation studies to demonstrate the effectiveness of the key components of our FlowLUT approach. The evaluation of these ablation experiments is conducted on the Mobile-Spec dataset.

Effectiveness of num LUTs and flow steps. The core of our FlowLUT framework relies on two critical hyperparameters: the number of specialized look-up tables (num_luts) and the number of iterative refinement steps in the flow matching module (flow_steps). We analyze their impact to find a balance between model capacity and computational overhead. As detailed in Table III, our empirical analysis reveals that the optimal configuration is achieved with 8 LUTs and 4 flow steps. While increasing these parameters initially boosts performance, further expansion results in diminishing returns and potential performance degradation, establishing this balance as the most effective trade-off for our model.

Effectiveness of the flow matching method. To validate the effectiveness of the flow matching module, we removed it in an ablation study. The results (as shown in Table II) indicate a sharp deterioration in model performance: the image quality metrics (PSNR, SSIM) dropped significantly, while the perceptual error (LPIPS) and color difference error (CIEDE) increased markedly.

Effectiveness of specialized LUTs. The foundation of our global enhancement stage is the ensemble of specialized, differentiable 3D LUTs, which provides a diverse set of color transformations. We tested its importance by replacing the entire ensemble of 8 specialized LUTs with a single, generic 3D LUT. The results, comparing Group (a) to Group (e) in Table II, demonstrate that this component is fundamental to our method's performance.

Effectiveness of perceptual loss. Our model is optimized with a composite loss function that includes an LPIPS perceptual loss to ensure the results align with human visual perception,

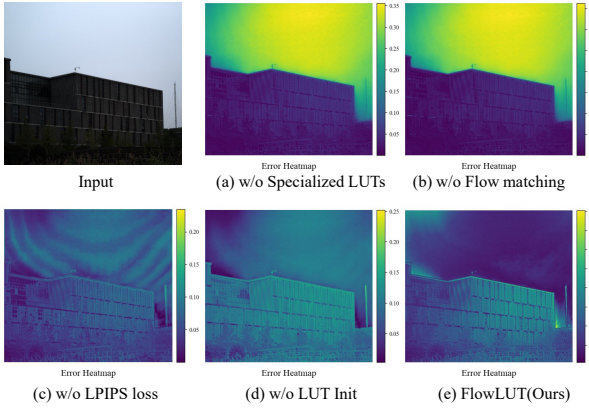


Fig. 6. Qualitative analysis of the ablation study on the Mobile-Spec dataset using L2 error heatmaps. This figure dissects the contributions of the model’s components by visualizing the spatial distribution and magnitude of the L2 error between the model’s output and the ground truth. The analysis shows that the full FlowLUT model exhibits the lowest overall error, visually validating the synergistic efficacy of the proposed architecture.

TABLE IV

COMPARISON OF RUNNING TIME (IN MILLISECONDS), COMPUTATIONAL COMPLEXITY (GFLOPS, GMACs), AND NUMBER OF PARAMETERS (#PARAMS(M)) OF FLOWLUT (OURS) AGAINST OTHER STATE-OF-THE-ART METHODS ON 1920 × 1080 RESOLUTIONS IMAGES.

Methods	Time(ms)↓	GFLOPs↓	GMACs↓	#Params(M) ↓
DnLUT	23.5	473.13	236.56	25.7
RetinexFormer	17.21	78.32	39.16	6.75
LightenDiffusion	840.18	104.27	52.14	23.7
CSEC	18.58	96.36	48.17	6.81
FlowLUT (Ours)	5.3	41.61	20.80	2.08

complementing the pixel-wise accuracy of the MSE loss. To verify its contribution, we trained a variant of our model using only the MSE loss. The comparison between this model (Group c) and our full model (Group e) in Table II reveals the importance of perceptual feedback.

Effectiveness of LUT initialization strategy. We employ a physically-inspired initialization strategy to provide the LUTs with meaningful priors, such as gamma correction and color temperature shifts, to guide the optimization process effectively. We evaluated this strategy by training a model where all LUTs were initialized as identity transformations. As shown in Table II, comparing this variant (Group d) with the full model (Group e), the lack of proper initialization leads to a clear drop in performance across all metrics.

V. DISCUSSION

A. Heat map of the errors.

To visually dissect the contributions of our model’s components, we present a qualitative analysis via error heatmaps in Figure 6, which correspond to the ablation experiments on the Mobile-Spec dataset. These visualizations map the spatial distribution and magnitude of the L2 error between the model’s output and the ground truth. Fig. 6(a) reveals that without the specialized LUTs, significant errors are concentrated in the sky region, indicating a failure to accurately model global color and tonal gradients. The removal of the Flow Matching module, as shown in Fig. 6(b), results in high-frequency errors across the building’s facade, underscoring its critical

role in refining structural details that the global LUTs cannot address. Similarly, training without the LPIPS loss (Fig. 6(c)) or our proposed LUT initialization (Fig. 6(d)) leads to diffusely higher error across the entire image, confirming their importance for perceptual fidelity and effective optimization convergence. In stark contrast, the full FlowLUT model (Fig. 6(e)) exhibits the lowest overall error, with residual inaccuracies being minimal and less structurally correlated, thereby visually validating the synergistic efficacy of our proposed architecture.

B. Computational efficiency

An analysis of computational efficiency, performed on images at a 1920 × 1080 resolution, confirms the superiority of the proposed FlowLUT method. As detailed in Table IV, FlowLUT exhibits a significantly reduced runtime (5.3 ms), operational complexity (41.61 GFLOPs), and model size (2.08M parameters) when benchmarked against other state-of-the-art approaches.

The model’s performance is particularly noteworthy; its runtime is substantially faster than all competitors, including being over 158 times faster than the diffusion-based Lighten Diffusion model. Moreover, its parameter count is less than a third of the next smallest competing models, underscoring its exceptionally lightweight design. This high efficiency is a direct consequence of the model’s architecture, which synergizes the $\mathcal{O}(1)$ complexity of Look-Up Tables for global enhancement with a parameter-efficient flow matching module for local, detailed refinement. This strategic combination of components establishes FlowLUT as a robust and practical solution for high-quality [39], real-time image enhancement, especially for deployment on resource-constrained platforms.

C. Flow path visualization.

To provide a transparent and intuitive understanding of the iterative refinement process within our FlowLUT framework, we visualize the step-by-step transformation of an image from its initial LUT-enhanced state to the final refined output. As illustrated in Fig. 7, the visualization demonstrates the progressive nature of the Flow Matching Refinement module. In the initial steps (step 1 and step 2), the model makes substantial corrections, focusing on gross artifact removal and the restoration of prominent structural features that were inadequately handled by the global LUT transformation. As the process advances through subsequent steps (step 3 and step 4), the refinements become increasingly subtle. The model then concentrates on recovering fine-grained textural details and ensuring local color consistency, gradually converging towards the ground truth. This visualization makes tangible the geometric interpretation of our refinement module as a form of gradient descent in the image space, where each step incrementally minimizes the residual error, leading to a perceptually high-quality result.

D. Mobile Deployment

To validate the practical applicability and efficiency of our framework in real-world scenarios, we deployed the FlowLUT



Fig. 7. Visualization of the iterative flow matching refinement process. This figure illustrates the progressive transformation from the initial LUT-enhanced image to the final output.

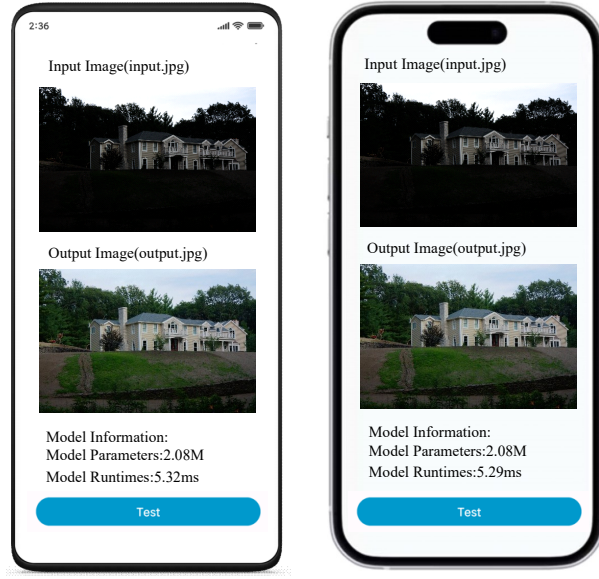


Fig. 8. Mobile deployment. On-device results on Huawei and Apple. The figure showcases a successful low-light enhancement scenario. A severely underexposed input image is restored to a well-lit and detailed output, demonstrating the FlowLUT's effectiveness in correcting extreme lighting conditions on mobile platforms.

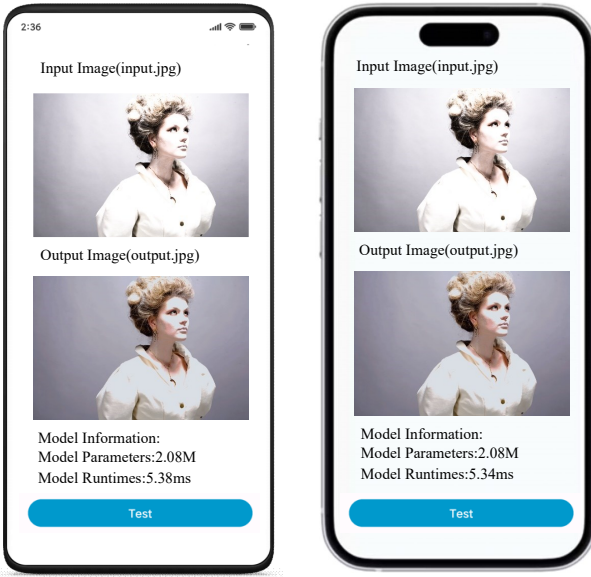


Fig. 9. Mobile deployment. On-device results on Huawei and Apple. This figure illustrates a more challenging case involving portrait enhancement. The input image presents a difficult lighting situation with a noticeable color cast. While the model significantly improves the overall brightness and color balance, it points to the complexities of achieving perfect color fidelity and detail restoration in specialized scenarios like portraiture under adverse conditions, representing an area for future refinement.

model on mainstream Huawei and Apple smartphones. This evaluation is critical to demonstrate its suitability for real-time

image enhancement on resource-constrained mobile devices. The deployment tests confirm that FlowLUT is exceptionally lightweight, with a total of only 2.08M parameters. This compact model size is crucial for on-device applications where memory and storage are limited.

As shown in Fig. 8 and 9, the model exhibits remarkable cross-device performance, achieving real-time inference speeds with runtimes of approximately 5.32ms on Huawei and 5.29ms on Apple for the first test case, and 5.38ms and 5.34ms respectively for the second. Fig. 8 provides a clear example of the model's success, effectively restoring visibility and detail in a severely underexposed image. In contrast, Fig. 9 presents a failure case where the model, despite improving a portrait with a strong color cast, does not achieve perfect color and detail restoration, highlighting the remaining challenges in handling complex portrait lighting. Collectively, these deployment results underscore FlowLUT's potential as a robust and efficient solution for on-device image enhancement, successfully balancing computational performance with high-quality restoration capabilities, though with identified areas for continued improvement in specific, complex cases.

VI. CONCLUSION

In this work, we introduced FlowLUT, a novel framework reconciling the trade-off between computational efficiency and representational capacity in image enhancement. Extensive experiments demonstrate that FlowLUT achieves state-of-the-art performance on multiple benchmarks, delivering visually superior results with remarkable computational efficiency. Additionally, we propose the use of an error heat map as an auxiliary method to more intuitively demonstrate the superiority of the FlowLUT model. Ultimately, FlowLUT presents a robust and practical solution for high-quality, real-time image enhancement.

REFERENCES

- [1] L. Ma, R. Liu, Y. Wang, X. Fan, and Z. Luo, "Low-light image enhancement via self-reinforced retinex projection model," *IEEE Transactions on Multimedia*, vol. 25, pp. 3573–3586, 2023.
- [2] S. Sun, W. Ren, T. Wang, and X. Cao, "Rethinking image restoration for object detection," in *Advances in Neural Information Processing Systems*, S. Koyejo, S. Mohamed, A. Agarwal, D. Belgrave, K. Cho, and A. Oh, Eds., vol. 35. Curran Associates, Inc., 2022, pp. 4461–4474. [Online]. Available: https://proceedings.neurips.cc/paper_files/paper/2022/file/1cac8326ce3fbe79171db9754211530c-Paper-Conference.pdf
- [3] Y. Chen, L. Yu, J.-Y. Wang, N. Panjwani, J.-P. Obeid, W. Liu, L. Liu, N. Kovalchuk, M. F. Gensheimer, L. K. Vitzthum, B. M. Beadle, D. T. Chang, Q.-T. Le, B. Han, and L. Xing, "Adaptive region-specific loss for improved medical image segmentation," *IEEE Transactions on Pattern Analysis and Machine Intelligence*, vol. 45, no. 11, pp. 13 408–13 421, 2023.
- [4] H. Rashed, M. Ramzy, V. Vaquero, A. El Sallab, G. Sistu, and S. Yoganmani, "Fusemodnet: Real-time camera and lidar based moving object detection for robust low-light autonomous driving," in *Proceedings of the IEEE/CVF international conference on computer vision workshops*, 2019.

[5] M. V. Conde, F. Vasluiu, J. Vazquez-Corral, and R. Timofte, "Perceptual image enhancement for smartphone real-time applications," in *Proceedings of the IEEE/CVF Winter Conference on Applications of Computer Vision*, 2023, pp. 1848–1858.

[6] H. Zeng, J. Cai, L. Li, Z. Cao, and L. Zhang, "Learning image-adaptive 3d lookup tables for high performance photo enhancement in real-time," *IEEE Transactions on Pattern Analysis and Machine Intelligence*, p. 1–1, 2020. [Online]. Available: <http://dx.doi.org/10.1109/TPAMI.2020.3026740>

[7] J. Liu, Q. Li, X. Min, Y. Su, G. Zhai, and X. Yang, "Pixel-learnable 3dlut with saturation-aware compensation for image enhancement," *IEEE Transactions on Multimedia*, vol. 26, pp. 11 219–11 231, 2024.

[8] K. Zuiderveld, *Contrast limited adaptive histogram equalization*. USA: Academic Press Professional, Inc., 1994, p. 474–485.

[9] C. Yang, M. Jin, X. Jia, Y. Xu, and Y. Chen, "Adaint: Learning adaptive intervals for 3d lookup tables on real-time image enhancement," in *Proceedings of the IEEE/CVF Conference on Computer Vision and Pattern Recognition*, 2022, pp. 17 522–17 531.

[10] T. Wang, Y. Li, J. Peng, Y. Ma, X. Wang, F. Song, and Y. Yan, "Real-time image enhancer via learnable spatial-aware 3d lookup tables," in *Proceedings of the IEEE/CVF International Conference on Computer Vision*, 2021, pp. 2471–2480.

[11] M. Gharbi, J. Chen, J. T. Barron, S. W. Hasinoff, and F. Durand, "Deep bilateral learning for real-time image enhancement," *ACM Transactions on Graphics*, vol. 36, no. 4, p. 1–12, Jul. 2017. [Online]. Available: <http://dx.doi.org/10.1145/3072959.3073592>

[12] J. Liu, G. Liu, J. Liang, Y. Li, J. Liu, X. Wang, P. Wan, D. Zhang, and W. Ouyang, "Flow-grpo: Training flow matching models via online rl," *arXiv preprint arXiv:2505.05470*, 2025.

[13] Z. Geng, M. Deng, X. Bai, J. Z. Kolter, and K. He, "Mean flows for one-step generative modeling," *arXiv preprint arXiv:2505.13447*, 2025.

[14] O. Ronneberger, P. Fischer, and T. Brox, "U-net: Convolutional networks for biomedical image segmentation," in *International Conference on Medical image computing and computer-assisted intervention*. Springer, 2015, pp. 234–241.

[15] S. W. Zamir, A. Arora, S. Khan, M. Hayat, F. S. Khan, and M.-H. Yang, "Restormer: Efficient transformer for high-resolution image restoration," in *Proceedings of the IEEE/CVF conference on computer vision and pattern recognition*, 2022, pp. 5728–5739.

[16] L. Nie, C. Lin, K. Liao, S. Liu, and Y. Zhao, "Parallax-tolerant unsupervised deep image stitching," in *Proceedings of the IEEE/CVF international conference on computer vision*, 2023, pp. 7399–7408.

[17] Y. Shi, K. Wang, C. Chen, L. Xu, and L. Lin, "Structure-preserving image super-resolution via contextualized multitask learning," *IEEE Transactions on Multimedia*, vol. 19, no. 12, pp. 2804–2815, 2017.

[18] H. Zeng, J. Cai, L. Li, Z. Cao, and L. Zhang, "Learning image-adaptive 3d lookup tables for high performance photo enhancement in real-time," *IEEE Transactions on Pattern Analysis and Machine Intelligence*, p. 1–1, 2020. [Online]. Available: <http://dx.doi.org/10.1109/TPAMI.2020.3026740>

[19] C. Yang, M. Jin, Y. Xu, R. Zhang, Y. Chen, and H. Liu, "Seplut: Separable image-adaptive lookup tables for real-time image enhancement," in *European Conference on Computer Vision*. Springer, 2022, pp. 201–217.

[20] T. Wang, Y. Li, J. Peng, Y. Ma, X. Wang, F. Song, and Y. Yan, "Real-time image enhancer via learnable spatial-aware 3d lookup tables," in *Proceedings of the IEEE/CVF International Conference on Computer Vision*, 2021, pp. 2471–2480.

[21] Y. Lipman, R. T. Q. Chen, H. Ben-Hamu, M. Nickel, and M. Le, "Flow matching for generative modeling," in *The Eleventh International Conference on Learning Representations*, 2023. [Online]. Available: <https://openreview.net/forum?id=PqvMRDCJ9t>

[22] P. Esser, S. Kulal, A. Blattmann, R. Entezari, J. Müller, H. Saini, Y. Levi, D. Lorenz, A. Sauer, F. Boesel *et al.*, "Scaling rectified flow transformers for high-resolution image synthesis," in *Forty-first international conference on machine learning*, 2024.

[23] A. Ramesh, P. Dhariwal, A. Nichol, C. Chu, and M. Chen, "Hierarchical text-conditional image generation with CLIP latents," *CoRR*, vol. abs/2204.06125, 2022. [Online]. Available: <https://doi.org/10.48550/arXiv.2204.06125>

[24] J.-H. Yun, S.-B. Kim, and S.-W. Lee, "Flowhigh: Towards efficient and high-quality audio super-resolution with single-step flow matching," in *ICASSP 2025 - 2025 IEEE International Conference on Acoustics, Speech and Signal Processing (ICASSP)*, 2025, pp. 1–5.

[25] C.-Y. Tsai, "A fast dynamic range compression with local contrast preservation algorithm and its application to real-time video enhancement," *IEEE Transactions on Multimedia*, vol. 14, no. 4, pp. 1140–1152, 2012.

[26] Z.-S. Liu, C. He, and L. Li, "Efficient point clouds upsampling via flow matching," 2025. [Online]. Available: <https://arxiv.org/abs/2501.15286>

[27] S. Sun, Y. Zhang, C. Wu, D. Lu, D. Lu, G. Zhan, Y. Weng, and Z. Zheng, "Uniflowrestore: A general video restoration framework via flow matching and prompt guidance," 2025. [Online]. Available: <https://arxiv.org/abs/2504.09069>

[28] X. Liu, C. Gong, and qiang liu, "Flow straight and fast: Learning to generate and transfer data with rectified flow," in *The Eleventh International Conference on Learning Representations*, 2023. [Online]. Available: <https://openreview.net/forum?id=XVjTT1nw5z>

[29] D. Jobson, Z. Rahman, and G. Woodell, "A multiscale retinex for bridging the gap between color images and the human observation of scenes," *IEEE Transactions on Image Processing*, vol. 6, no. 7, pp. 965–976, 1997.

[30] A. R. Smith, "Color gamut transform pairs," *SIGGRAPH Comput. Graph.*, vol. 12, no. 3, p. 12–19, Aug. 1978. [Online]. Available: <https://doi.org/10.1145/965139.807361>

[31] H. Cheng, X. Jiang, Y. Sun, and J. Wang, "Color image segmentation: advances and prospects," *Pattern Recognition*, vol. 34, no. 12, pp. 2259–2281, 2001. [Online]. Available: <https://www.sciencedirect.com/science/article/pii/S0031320300001497>

[32] Z. Zhu, M. Toyoura, K. Go, K. Kashiwagi, I. Fujishiro, T.-T. Wong, and X. Mao, "Personalized image recoloring for color vision deficiency compensation," *IEEE Transactions on Multimedia*, vol. 24, pp. 1721–1734, 2022.

[33] H. Wang, K. Xu, and R. W. H. Lau, "Local color distributions prior for image enhancement," *Springer, Cham*, 2022.

[34] K. Zhou, L. Cai, Y. Wang, M. Zhang, B. Wen, Q. Shen, and X. Cao, "Joint rgb-spectral decomposition model guided image enhancement in mobile photography," in *European Conference on Computer Vision*, 2025.

[35] N. Jiang, W. Chen, Y. Lin, T. Zhao, and C.-W. Lin, "Underwater image enhancement with lightweight cascaded network," *IEEE Transactions on Multimedia*, vol. 24, pp. 4301–4313, 2022.

[36] L. Peng, C. Zhu, and L. Bian, "U-shape transformer for underwater image enhancement," *IEEE Transactions on Image Processing*, vol. 32, pp. 3066–3079, 2023.

[37] Z. Wang, A. C. Bovik, H. R. Sheikh, and E. P. Simoncelli, "Image quality assessment: from error visibility to structural similarity," *IEEE Trans Image Process*, vol. 13, no. 4, 2004.

[38] R. Zhang, P. Isola, A. A. Efros, E. Shechtman, and O. Wang, "The unreasonable effectiveness of deep features as a perceptual metric," in *Proceedings of the IEEE conference on computer vision and pattern recognition*, 2018, pp. 586–595.

[39] R. Verhach, T. Sikora, G. Van Wallendael, and P. Lambert, "Steered mixture-of-experts for light field images and video: Representation and coding," *IEEE Transactions on Multimedia*, vol. 22, no. 3, pp. 579–593, 2020.

[40] G. Sharma, W. Wu, and E. N. Dalal, "The ciede2000 color-difference formula: Implementation notes, supplementary test data, and mathematical observations," *Color Research Application*, vol. 30, no. 1, pp. 21–30, 2010.

[41] R. Liu, L. Ma, J. Zhang, X. Fan, and Z. Luo, "Retinex-inspired unrolling with cooperative prior architecture search for low-light image enhancement," in *Proceedings of the IEEE/CVF conference on computer vision and pattern recognition*, 2021, pp. 10 561–10 570.

[42] Y. Cai, H. Bian, J. Lin, H. Wang, R. Timofte, and Y. Zhang, "Retinexformer: One-stage retinex-based transformer for low-light image enhancement," in *Proceedings of the IEEE/CVF international conference on computer vision*, 2023, pp. 12 504–12 513.

[43] S. Yang, B. Huang, Y. Zhang, D. Yu, Y. Yang, and N. Wong, "Dnlut: Ultra-efficient color image denoising via channel-aware lookup tables," in *Proceedings of the Computer Vision and Pattern Recognition Conference*, 2025, pp. 7582–7591.

[44] H. Jiang, A. Luo, X. Liu, S. Han, and S. Liu, "Lightendiffusion: Unsupervised low-light image enhancement with latent-retinex diffusion models," in *European Conference on Computer Vision*. Springer, 2024, pp. 161–179.

[45] Y. Li, K. Xu, G. P. Hancke, and R. W. Lau, "Color shift estimation-and-correction for image enhancement," in *Proceedings of the IEEE/CVF Conference on Computer Vision and Pattern Recognition*, 2024, pp. 25 389–25 398.

[46] R. Pucci and N. Martinel, "Ce-vae: Capsule enhanced variational autoencoder for underwater image enhancement," in *2025 IEEE/CVF Winter Conference on Applications of Computer Vision (WACV)*, 2025, pp. 2113–2123.